University of Groningen

Structure and reconfiguration of epitaxial GeTe/Sb2Te3 superlattices

Momand, Jama

IMPORTANT NOTE: You are advised to consult the publisher's version (publisher's PDF) if you wish to cite from it. Please check the document version below.

Document Version
Publisher's PDF, also known as Version of record

Publication date:
2017

Experimental Methods

"It is poor comfort to hope that human ingenuity will find ways and means of overcoming this [optical resolution] limit." – Ernst Abbe

Abstract

The first part of this chapter treats some of the general aspects of transmission electron microscopy which are relevant for the work in this thesis. This includes conventional transmission electron microscopy and scanning transmission electron microscopy. The second part then continues with specimen preparation, which is equally important to obtain useful results and meaningful analyses. In the end the specific specimen preparation recipes are outlined, which could be used as a reference for future work.

---

‡ *Parts of section 2.1.2 of this chapter have been published in the supplementary information of Momand, J. et al. Dynamic reconfiguration of van der Waals gaps within GeTe–Sb$_2$Te$_3$ based superlattices. Nanoscale 9, 8774–8780 (2017).*

2.1 Electron microscopy

The exciting field of microscopy concerns itself with the study of the micro-world and goes back to at least the 17th century.[1] Then Antonie van Leeuwenhoek used the first optical microscope to study cells and bacteria, achieving a resolution of less than 1 μm. The field then further developed and matured, finding the optical resolution limit, Abbe's limit, at the end of the 18th century. This prompted Ernst Abbe to complain about this, as written in the beginning of this chapter, and posed a fundamental boundary to what could be achieved with optics. However, it was discovered by Louis de Broglie, some 20 years after Abbe's death, that electrons too have a wave character. Not much later, March 9th 1931, the first electron microscope was designed by Ernst Ruska and it was first used in the paper of him together with Knoll in 1932.[2,3] In the same year the optical resolution limit was surpassed and it was this development of the electron microscope for which Ruska received a Nobel prize in 1986.
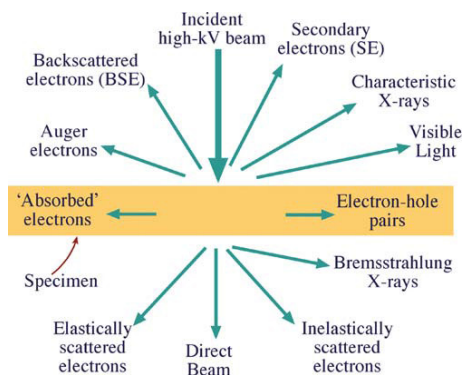
Figure 2.1*: Interaction of a high-energy electron beam with matter. The directions shown for each signal are schematically drawn and do not always represent the physical direction of the signal. Adapted from Williams and Carter.[2]*

Nowadays high-energy electron techniques are of paramount importance for materials characterization. Figure 2.1 shows schematically the type of interactions high-kV electron beams have with matter. When high-energy electrons travel through a crystal, they respond to the crystal potential. Due to potential differences they acquire a shift in their phase in the direct beam, which can be used for phase-contrast imaging. The electrons can also scatter and diffract due to the periodicity

of the crystal, leading to elastically and inelastically scattered beams which may be used for diffraction or SE, BSE and diffraction contrast imaging. The beam can also knock-off the atomic inner-shell electrons, of which the fall back of higher-shell electrons gives rise to element specific characteristic X-rays and Auger processes. If the electrons are decelerated by the potential, this gives rise to "bremsstrahlung" or X-rays, which is typically a background signal in X-ray spectra. These and many other interactions, like excitonic or plasmonic excitations, lead to characterization techniques in the list below:

- Bright-Field/Dark-Field (BF/DF) Transmission Electron Microscopy (TEM)
- Scanning Transmission Electron Microscopy (STEM)
- Selected Area Electron Diffraction (SAED)
- Energy Dispersive X-ray spectroscopy (EDXS)
- Electron Energy Loss Spectroscopy (EELS)
- SE/BSE Scanning Electron Microscopy (SEM)
- Auger Electron Spectroscopy (AES)

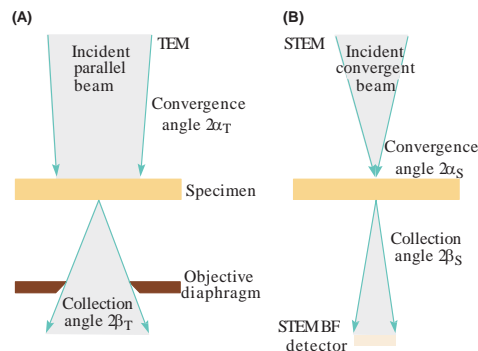Typically many techniques can be combined in one instrument, such as TEM/STEM/SAED/EDXS/EELS in one TEM.

Figure 2.2: *Comparison of the important beam-convergence and divergence angles (A) in TEM and (B) in STEM. Adapted from Williams and Carter.[2]*

This thesis depends particularly on TEM and STEM characterization, with occasionally using SAED and EDXS. Figure 2.2 shows a schematic of both

techniques, where the primary difference is that in TEM, Figure 2.2 (A), the image is formed by an incident parallel beam, while for STEM, Figure 2.2 (B), the image is formed by scanning a small probe over the specimen and collecting the scattered electrons. Modern TEM and STEM instruments could have additional image and probe correctors, but these will not be treated here.

The fundamental limit of microscopy resolution δ_{th}, which is usually defined as the ability to resolve two separate points of an object that are located at a small angular distance from each other, is given by Equations 2.1.a and 2.1.b, where λ and β are the wavelength and collection semi-angle, respectively.[2]

$$\delta_{th} = \frac{0.61\lambda}{\sin\beta} \tag{2.1.a}$$

$$\delta_{th} \approx \frac{0.61\lambda}{\beta} \; for \; \beta \ll 1$$

$$\delta_{th} \approx 0.61\lambda \; for \; \beta \approx \frac{\pi}{2} \tag{2.1.b}$$

For optical microscopy Equation 2.1.b typically gives a resolution $\delta_{th} \sim 300$ nm for green $\lambda \sim 500$ nm light. This would be better for higher energy photons, but the problem is that it is not possible to produce X-ray lenses. For electrons, however, the wavelength λ is much shorter and can be calculated by the relation given in Equation 2.2. Here, h is Planck's constant, m_0 is the electron rest mass, e the electron charge, c the speed of light and V the accelerating voltage. These are the relativistic and classical expressions, respectively, and they are plotted in Figure 2.3. It can be read of that the classical and relativistic expressions for the wavelength λ differ no more than an order of magnitude for $V < 100$ MV, so that typically the classical expression can be used. For typical S/TEM instruments the accelerating voltage V is around 200 kV, giving $\lambda \sim 2.5$ pm, which is five orders of magnitude lower than for visible light. Therefore, with sufficient engineering, electrons could ideally be used to study the real-space atomic structure of materials, which require $\delta \sim 0.3$ nm. In the literature one can find examples of modern instruments where single C atoms can be resolved in free-standing graphene[4] or H atomic columns in yttrium hydride.[5]

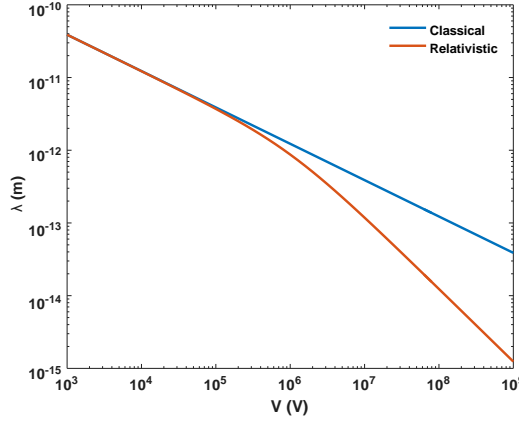$$\lambda = \frac{h}{\sqrt{2m_0eV(1 + \frac{eV}{2m_0c^2})}} \approx \frac{h}{\sqrt{2m_0eV}} \qquad (2.2)$$

Figure 2.3: *Electron wavelength λ versus the accelerating voltage V. It can be seen that until 10^8 eV or 100 MeV the classical and relativistic expressions for λ differ no more than one order of magnitude.*

Unlike for optical lenses, where the quality can be made to such an extent that their resolution is limited by Equation 2.1, electron lenses are rather limited by imperfections which yield spherical (C_s) and chromatic (C_c) aberrations.[2] Equation 2.3 gives the resolution limitation due to this spherical aberration C_s, which has typical dimensions of 1 mm for e.g. JEOL 2010 or 2010F, which are used for parts of this thesis. The second term added is the effect of defocus, which is the deviation of the focus setting from the ideal focus $\Delta f = f - f_0$.

$$\delta_{Cs} = C_s\beta^3 + \Delta f\beta \qquad (2.3)$$

To give an estimate of the conditions for the best resolution δ, one could assume that δ_{th} and δ_{Cs} are independent and minimize $\delta^2 = (\delta_{th})^2 + (\delta_{Cs})^2$ at zero defocus Δf, which leads to Equation 2.4.

$$\beta = 0.77\, C_s^{-1/4}\lambda^{1/4}$$
$$\delta = 0.91\, C_s^{1/4}\lambda^{3/4} \qquad (2.4)$$

This gives $\beta \sim 5.5$ mrad and $\delta \sim 0.32$ nm for a TEM operated at 200 kV and a C_s of 1 mm. Sometimes for simplicity Equations 2.1 and 2.3 are just equated with each other $\delta_{th} = \delta_{Cs}$, which results in Equation 2.5.

$$\beta = 0.88 \, C_s^{-1/4} \lambda^{1/4}$$
$$\delta = 0.69 \, C_s^{1/4} \lambda^{3/4}$$

(2.5)

This gives $\beta \sim 6.3$ mrad and $\delta \sim 0.24$ nm for a TEM operated at 200 kV and a C_s of 1 mm. Both Equations 2.4 and 2.5 give slightly higher point-resolution values than provided by the manufacturer of the JEOL 2010 and 2010F microscopes, $\delta \sim 0.23$ nm, but they are good estimates.

For objects much larger than this resolution limit, the contrast formation is typically due to scattering of electrons and interpretation is straightforward. However, images near the resolution of the microscope are formed by phase contrast and simulation may be necessary. This will be discussed in the next section.

2.1.1 High-Resolution Transmission Electron Microscopy

The previous approximations of the resolution give a general indication of the possibility to resolve details in a material. But to further understand the image formation mechanism in TEM there are the general problems that (*i*) the lens system is not perfect and has a finite size and (*ii*) the exact atomic potential and bonding of the studied material is not known. Nevertheless, to understand the signals which are generated in the instrument, the study of contrast formation mechanisms is described by the information theory for high-resolution TEM (HRTEM).[2] Here, the process of TEM analysis is described by linear signal theory, which is justified due to the linearity of the Schrödinger equation. The image function *g(r)* is formed by a convolution of the TEM's Contrast Transfer Function (CTF) *h(r)* and the specimen transmission function *f(r)*, see Equation 2.7, Since the convolution is a multiplication in Fourier space, the image function *G(u)* can be written as a multiplication of *F(u)* and *H(u)*.

$$g(r) = f(\boldsymbol{r}) \otimes h(\boldsymbol{r} - \boldsymbol{r}')$$
$$G(\boldsymbol{u}) = F(\boldsymbol{u})H(\boldsymbol{u}) \tag{2.7}$$

If the specimen is very thin the contrast formation can be described in the so called Weak Phase Object approximation. Then the CTF is given by the sine of the phase-distortion function $\chi(\boldsymbol{u})$, the $2\pi/\lambda$ integrated Equation 2.3 where $\beta = \lambda\, u$, as shown by Equations 2.8 and 2.9. Figure 2.4 shows the CTF H(u) for $V = 200$ kV and $C_s = 1$ mm using different Δf.

$$\chi(\boldsymbol{u}) = \pi\, \Delta f\, \lambda\, u^2 + \frac{\pi}{2} C_s \lambda^3 u^4 \tag{2.8}$$

$$H(\boldsymbol{u}) \sim \sin(\chi(\boldsymbol{u})) = \sin(\pi\, \Delta f\, \lambda\, u^2 + \frac{\pi}{2} C_s \lambda^3 u^4) \tag{2.9}$$
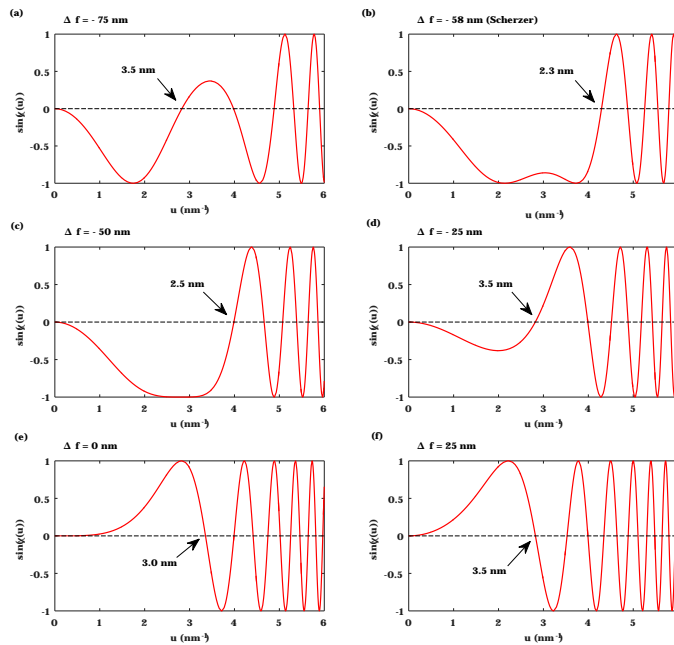

Figure 2.4: *Plots of the CTF H(**u**) for a 200 kV TEM with C_s = 1 mm. Different Δf are used as indicated above the plots. The black arrow indicates the first zero with corresponding real-space value.*

What can be extracted from this is that the high-resolution contrast formation mechanism in conventional HRTEM is formed by phase-contrast, while this does not play a role for objects much larger than the resolution limit. This is due to the relative shift of the phases of the electrons as they pass through the material. Also, when $H(\textbf{u})$ is negative, positive phase contrast results, meaning that atoms appear dark against a bright background, and vice versa (assuming positive C_s). Hence, since the CTF is oscillating through positive and negative values as the focus is changed, phase-contrast can enhance or hide certain details. This brings a tremendous difficulty, and probably one of the biggest challenges, to correctly interpret TEM images. Figure 2.5 shows a simulation of an Sb_2Te_3 crystal as seen in the [11-20] zone axis, where the Sb and Te atoms are indicated by green and blue circles, respectively. From this, it is clearly illustrated that (*i*) the contrast differs for different thicknesses and focus values and (*ii*) the spots in the image do not necessarily correspond to atomic positions.
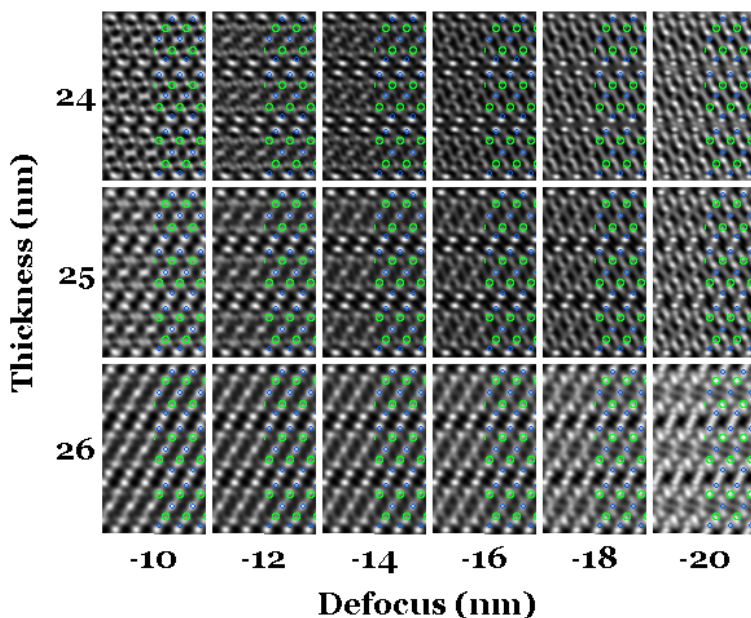

Figure 2.5: *Simulation of Sb_2Te_3 in the [11-20] zone axis as seen in a TEM for different thicknesses and different defocus values. The Sb and Te atom positions are indicated with green and blue circles, respectively. Simulated with MacTempas software package.*

Two additional comments can be made from the previous discussion:

First, one could define an optimal point resolution at the defocus value where one has a largest area of the transfer function and find the corresponding values of defocus and resolution. This was realized by Scherzer and can be done by e.g. solving the two equations d $\chi(\textbf{u})/du = 0$ and $\chi(\textbf{u}) = -2\pi/3$. In addition, by finding the numerical value of u at the first zero one arrives at Equation 2.10 for optimal defocus and resolution.

$$\Delta f_{Sch} = -\sqrt{\frac{4}{3} C_s \lambda}$$

$$\delta = 0.65\, C_s^{1/4} \lambda^{3/4}$$

(2.10)

Using the values $V = 200$ kV and $C_s = 1$ mm as before, this gives $\Delta f \sim -58$ nm and $\delta \sim 0.23$ nm. See also the CTF for the Scherzer defocus in Figure 2.4. Note that the estimations for the resolution from Equations 2.4, 2.5 and 2.10 are actually quite close.

Second, Figure 2.4 gives the impression that the CTF has a nonzero value for higher u and keeps oscillating. By recording data at multiple defocus values Δf one could retrieve information at values lower than the optimal resolution. However, in practice there is a cutoff for $H(\textbf{u})$ which is due to e.g. chromatic aberrations, source spread of angles, specimen drift, specimen vibration, detector limitations and objective aperture. This value lies typically further than the optimal point resolution δ_p and defines the information limit of the microscope. E.g. the JEOL 2010F which was used for parts of this thesis has a point resolution $\delta_p \sim 0.23$ nm, but an information limit $\delta_{inf} \sim 0.11$ nm.

2.1.2 Scanning Transmission Electron Microscopy

Nowadays modern TEMs are also equipped with STEM possibilities, where instead of using a wide parallel beam to record images, a small probe is scanned over the specimen. The transmitted and scattered electrons are then collected for different regions and mapped to form the micrograph. Figure 2.6 shows a schematic of the different STEM detectors, where the BF detector captures the transmitted electrons

while the Annular Dark-Field (ADF) and High-Angle Annular Dark Field (HAADF) detectors capture the electrons scattered at higher angles.
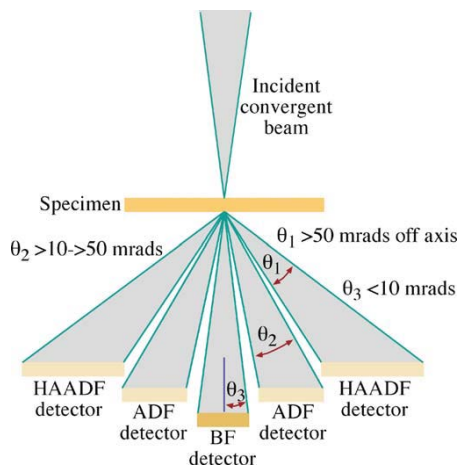

Figure 2.6: *Schematic of electron detectors in STEM mode. The approximate collection angles θ are also indicated in the image. Adapted from Williams and Carter.[2]*

Compared with TEM, STEM has many advantages. Even though the image formation mechanism for BF STEM is the same as for BF TEM, letting one of the giants in the field David Muller to call it "fake TEM", energy losses in the sample do not contribute to chromatic aberrations.[6] Therefore it becomes easier to resolve relatively thick specimen using STEM than TEM. Also, the electrons captured at higher angles like in ADF and HAADF become progressively more incoherent. This has a great advantage for interpretation, as phase-contrast does not enhance or hide details depending on the focus settings, as described in the previous section. Figure 2.7 (A) and (B) show the phase and amplitude CTF, respectively, as adapted from a presentation of David Muller. What can be observed from Figure 2.7 (A) is that for collecting angles < 10 mrad phase-contrast plays a significant role in the image formation. For higher angles the signal progressively attenuates till no phase-contrast is observed anymore after > 10 mrad. The amplitude contrast in Figure 2.7 (B) then shows that for higher collection angles > 10 mrad contrast reversals are removed and the resolution is increased, which has to do with the fact that the captured electrons are incoherent. Hence, STEM has the advantage of

easier imaging of thicker specimen and easier interpretation due to incoherent imaging.
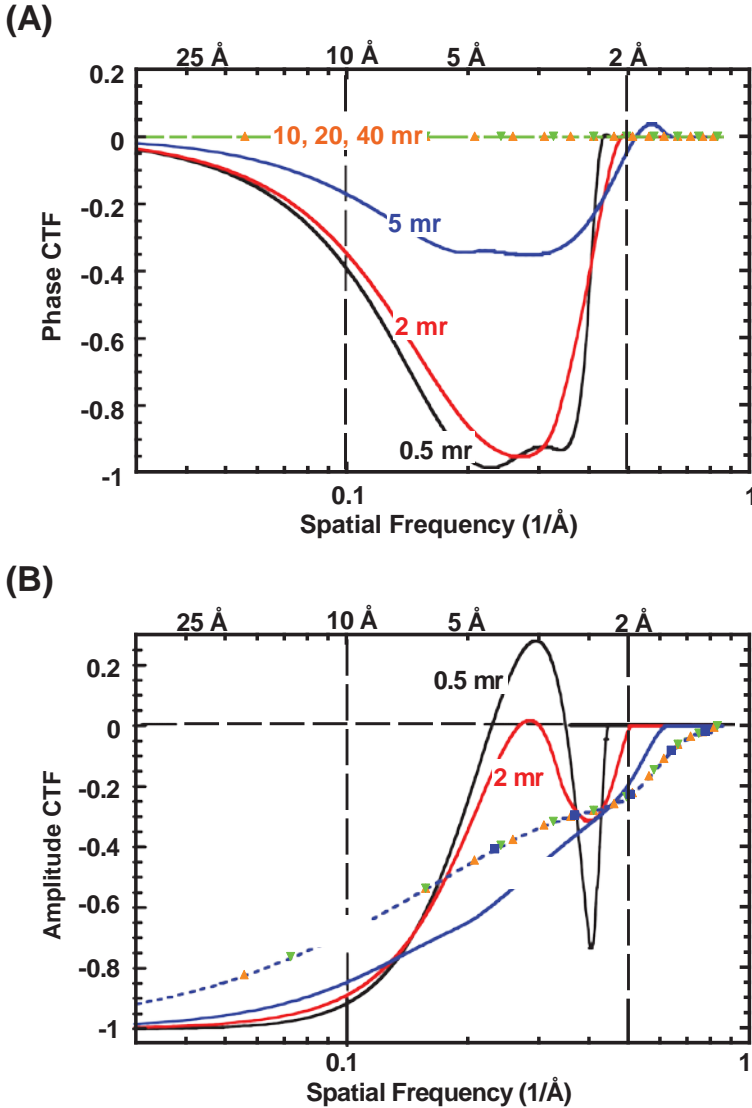

Figure 2.7: (A) Phase and (B) amplitude CTF for 10.5 mrad objective aperture, V = 200 kV and Cs = 1 mm at Scherzer defocus for different collection angles. Note that for angles > 10 mrad phase contrast disappears and mainly amplitude contrast contributes to the image. Adapted from a Cornell University 2006 Electron Microscopy Summer School presentation of David A. Muller.[6]

To give an example of how such interpretation is done for this thesis, see Figure 2.8 of a GeTe/Sb_2Te_3 heterostructure as studied in Chapter 4 of this thesis. Since the metastable and stable crystalline phases of GST have been widely studied using different experimental techniques including X-Ray Diffraction (XRD)[7–12] and (Scanning) Transmission Electron Microscopy ((S)TEM)[13–18], one can make some assumptions about its structure:

- Metastable GST has a distorted rocksalt structure where the anion lattice is fully (= 1) occupied by Te and the cation lattice is randomly occupied by Ge/Sb/vacancies.
- Stable GST is similar with the major differences that van der Waals (vdW) gaps have formed, containing adjacent Te-Te atomic planes in its stacking, and the distribution of Ge/Sb is such that the Sb-richer planes are closer to vdW gaps and Ge richer planes are at the centers of the blocks.
- Anti-site disorder is not significant in the stable phase of GST.
- The HAADF intensity scales approximately between $Z^{1.7}$ and Z^2.

Using these structural properties, HAADF-STEM micrographs of GST phases can qualitatively be interpreted without ambiguity, as for example shown in Figure 2.8 below.
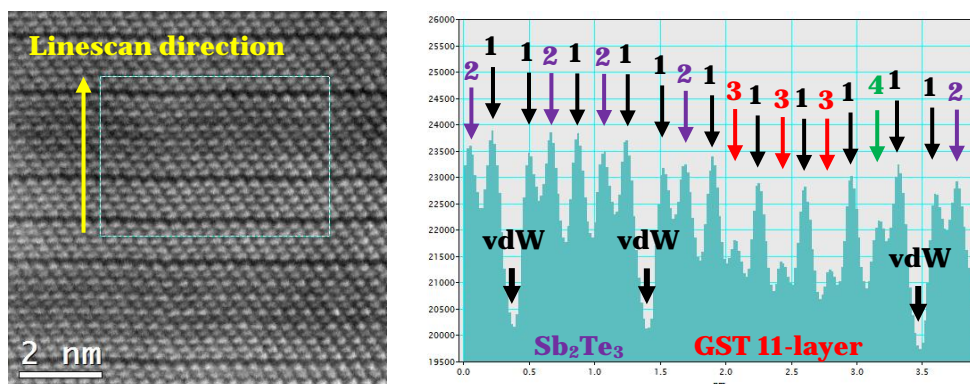

Figure 2.8: *Interpretation of HAADF-STEM micrographs (left) using intensity linescans (right).*

1. The atomic planes next to the vdW gaps, as well as every alternate anion atomic plane in the growth direction, must be close to pure Te planes (see black arrows). Note that the intensity is not fully homogeneous across the image. This is a specimen preparation artifact which can be due to specimen thickness variation and/or amorphous damage variation.

2. Adjacent to the Te must be Ge/Sb planes. Since the HAADF intensity scales with ~Z^2, where $Z_{Ge} = 32$, $Z_{Sb} = 51$ and $Z_{Te} = 52$, the other planes with intensities close to Te must be close to pure Sb (see purple arrows).

3. Due to deposition kinetics of superlattices the atomic planes with lowest intensities must be close to pure Ge (see red arrows).

4. The planes with intermediate intensities therefore must be mixed with Ge/Sb (see green arrow).

Looking across the linescan in Figure 2.8 (right) it becomes evident that the first vdW block is an Sb_2Te_3 quintuple layer and the second vdW block a GST 11-layer with a stacking sequence closely related to that proposed by Kooi *et al.* (Te-Sb-Te-Ge-Te-Ge-Te-Ge-Te-Sb-Te).[13] A more quantitative estimation of atomic species in GST using HAADF intensities should be done using simulations and can be found in other references in the literature.[14,16] So, HAADF-STEM is a very powerful technique for atomic resolution Z-contrast imaging, but still it will in a standard sense provide 2D projected images of 3D structures, although in the projection direction the thickness will not exceed a few tens of nanometers. Therefore it is important that the TEM specimen is oriented accurately with certain crystal directions parallel to the incident electron beams and this can be facilitated if it is possible to prepare the TEM specimen already in a preferred orientation as will be explained in more detail in the next section.

2.2 TEM specimen preparation

The preparation or TEM specimen out of material samples is an important and crucial task for the electron microscopist. Roughly speaking, the quality of your results is equal to the quality of your TEM multiplied by the quality of your specimen. So no matter how advanced and expensive your microscope is, without good specimen you will not be able to do good TEM analysis.

The topic of TEM specimen preparation is broad and a lot of documentation already exists in the literature, see e.g. Chapter 10 of the book of Williams and Carter[2] and the references therein. Therefore, in this part of the Experimental Methods some of the general techniques of TEM specimen preparation are only briefly discussed, after which the specific methods used for this thesis are outlined. The primary concern for such specimen in the TEM is that they should be electron-transparent, but also (preferably) uniformly thin, stable under the electron beam and in the laboratory environment, conducting and non-magnetic. This typically comes down to specimen with thicknesses of < 100 nm due to the strong interaction between electrons and matter. Materials do not behave ideally, and generally differently, in this respect and therefore the preparation of good specimen is an art in and of itself.

To make a sample electron transparent and suitable for the TEM one has to thin it using mechanical, ion-polishing or chemical etching methods. No need to say that this is frequently destroying (a part of) your sample and one has to be sure that in the end the specimen is still representative of the original material. One has to be aware of possible contaminations and artifacts which can occur and know how to avoid it if necessary. Figure 2.9 shows a general flowchart for possible preparation procedures, which was adapted from Williams and Carter.[2] Even though this chart is not complete it may be a good guideline for deciding which recipe you want to use. Ultimately the method applied depends on the information you need, time constraints, availability of equipment, your skill and the material sample itself. Some methods may be more time-consuming than the others, but the results and analyses may be worth the time.
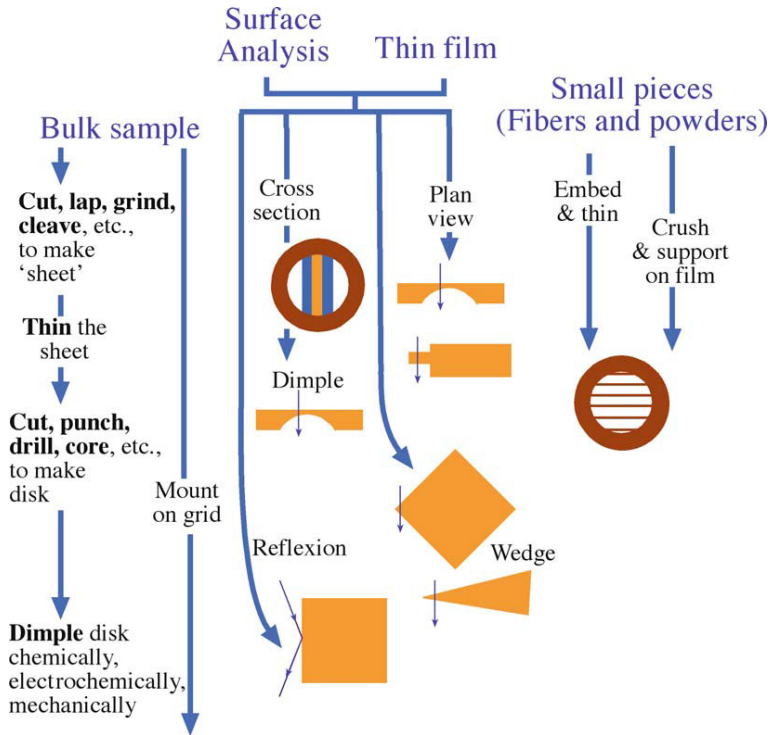
Figure 2.9*: Summary flow chart (incomplete) which can be used for deciding the TEM specimen preparation method. Adapted from Williams and Carter.[2]*

The type of artifacts induced in specimen frequently depends on the preparation method, assuming that the thin slice of material is not already reacting under ambient conditions when it is thinned down to tens of nanometers. It is known that e.g. mechanical preparation methods can induce defects and dislocations due to slip of atomic plane and ion-milling can amorphize the polished surface, adding undesired amorphous chunks of material to your specimen. A good illustration of these latter effects have been discussed by McCaffrey et al.,[19] see Figure 2.10. In that work it is shown that the surface damage and amorphization becomes progressively worse for cleavage, low-angle ion-milling, conventional ion-milling and preparation using the Focused Ion Beam (FIB). From this it becomes apparent that cleavage may be one of the best techniques for thin slices and this is an explanation of McCaffrey's successful method referred to as the Small Angle Cleavage Technique (SACT).[20,21] This method works well for semiconductors and can be applied to thin films.[22] It is not used in this thesis, however, because the

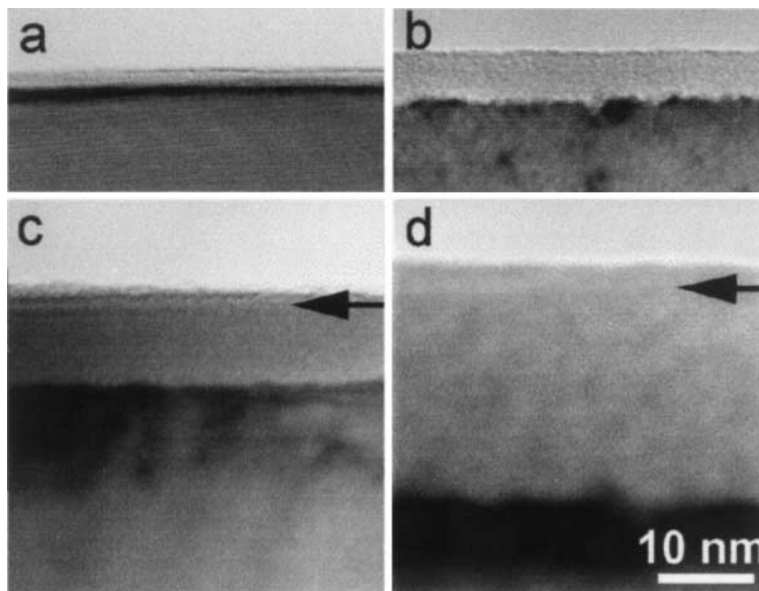studied thin films were layered with weaker planar bonding and could easily delaminate from the substrate.

Figure 2.10: *Surface amorphization of (a) cleavage, (b) low-angle ion-milling, (c) conventional ion-milling and (d) FIB preparation. Adapted from McCaffrey et al.[19]*

The FIB provides a high-tech preparation technique which has the advantage of being able to very locally, on the micrometer scale, select a desired piece of material for further study.[23–25] These instruments are very expensive, however, and the induced damage may be quite severe, as is shown by Figure 2.10 (d). Many examples are known of where the TEM region of interest is completely lost due to improper preparation. This even includes some examples within the Zernike Institute of Advanced Materials, where e.g. ~10 nm films were undetectable due to FIB preparation (not discussed here), which could be due to amorphization damage or non-expert usage. A lot of progress has nevertheless been made over the years and it is now possible to make a reasonable cross-section sample in the time frame of hours, which comes at a price. An additional problem is that most of the FIB instruments used for TEM specimen preparation use Ga ions and can contaminate parts of your region of interest.[19,23,24,26] Therefore, current state of the art FIB

specimen are prepared in combination with low-voltage Ar ion-milling to remove the amorphous damage and the Ga contaminated regions.[27,28]

2.2.1 Cross-sectional method used for this thesis

This and the next section discuss the specific methods of specimen preparation used for this thesis. All of the samples are thin films of GeTe, Sb_2Te_3 or GST superlattices on Si(111) substrates, which are studied in plan-view and cross-section. The basic methods can be read out from the flow-chart of Figure 2.9.
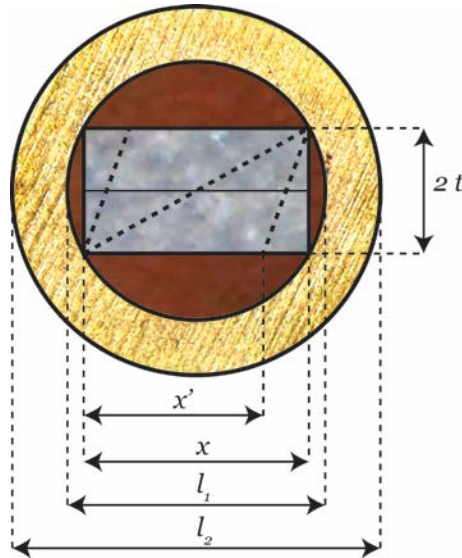

Figure 2.11: Design of cross-sectional TEM specimen out of thin film samples. The specimen consists of the Si substrate, brass tube support and epoxy resin binder.

The cross-sectional specimen preparation method is similar to the ones used in the literature for metallic substrates[29] and organic films.[30] The consecutive steps for this method are listed below. A design of the cross-sectional specimen is shown in Figure 2.11.

1. Measuring and logging the physical dimension of the thin film sample.
2. Cleaving the sample in ~1.5 mm long strips, depending on the thickness.
3. Gluing the strips to each other using Gatan G1 epoxy resin.
4. Gluing the scaffold from 3. into 3 mm Ø brass tubes.
5. Cutting the brass tubes into 0.5 mm thick disks.

6. Mechanical grinding of disks till ~100 μm thickness.
7. Dimple grinding of disks on both sides.
8. Ar ion-milling till a hole is visible.
9. Lower voltage ion-polishing.

Step 1 of the list seems to be obvious, but very essential. Here it is necessary to inspect the sample to identify the film-side, but also to check if a quick cleaning step is necessary (e.g. using acetone and isopropanol). Also, for step 2, the sample thickness is an important variable to determine the width of the strips to be cleaved or cut. Using the design from Figure 2.11 and denoting l_1 as the inner diameter of the target tube, the strips should be cleaved with a width x as given simply by Equation 2.11.

$$x = \sqrt{l_1^2 - 4t^2} \tag{2.11}$$

In step 2 such strips should preferably be cleave along the Si<1-10> directions, because the final specimen will end up in this zone-axis. This has many advantages, including being able to resolve the larger Si(111) and Si(200) lattice spacing for calibration purposes and, as will be shown in Chapter 6 of this thesis, due to the film's preferred crystallographic matching to this direction. Also, Si cleaves easier along <1-10> directions, which is also supported by theoretical literature studies.[31] However, the cleave plane is typically another (111) which is inclined at an angle θ = 19.47°, as is indicated by the dashed lines in Figure 2.11. Therefore, a certain amount of material should be subtracted from the width x to get x' as given by Equation 2.12. Typical sizes are l_1 = 2.1 mm and t = 0.5 mm, which gives x = 1.8 mm and x' = 1.5 mm.

$$x' = x - 2t \tan \theta \tag{2.12}$$

For step 3 the strips are glued together facing each other with the film side using Gatan G1 or G2 epoxy resins. These are specialized resins by the Gatan company,

which specializes at TEM applications, but also other commercially available resins should suffice. The important things to keep in mind are that the cured epoxy should have low outgassing properties in the vacuum, good ion-milling properties and not react under the influence of the electron beam. E.g. the EPO-TEK 353ND resins seems to have quite similar characteristics as Gatan G1 (at a substantially lower price).

For step 4 the scaffold is inserted into a tube after which it is slowly filled with the remainder of the epoxy. Note that if the curing should be done at higher temperatures, it is more convenient to fill the tube above a hot plate at a higher temperature, but not that high that it will be cured immediately. The higher temperature has an additional advantage of making the epoxy less viscous. This makes it easier to fill the tube from the side and avoid bubbles.

It is important for the final TEM specimen to have well cured epoxy support for specimen stability and contamination purposes inside the TEM. Nevertheless, this should be balanced against the other steps. When the tubes are cut into 0.5 mm disks, significant damage can be made to the Si substrate due to its brittleness. So, sometimes it can be better to cut it when the epoxy is relatively soft. But do not forget to finish the curing afterwards, as e.g. shown in Figure 2.12.

Figure 2.12: *Cut disks out of the brass tube. The epoxy used in this case is Gatan G1, which gets an amber color after the cure. As can be seen, the specimen on the left is not cured, while the two on the right are cured at progressively higher temperatures.*

In step 5 the tubes are cut into 0.5 mm disks using e.g. a low-speed diamond-wheel saw (excluding the thickness of the blade). As mentioned before, this step can damage the specimen and many precautions should be taken. E.g. softer epoxy,

lower cutting speed, lower weight on the blade, liquid cooling, etc. could be used and the cut should be performed such that the least amount of thickness is penetrated with the blade. This is typically with the cutting blade parallel to the glue-line or film-line. Also, a special holder or support for the tube is advisable, which makes sure that the cut is homogeneous. For the work in this thesis, special graphite holder were designed and made for cutting purposes.

To start step 6 it is important that the epoxy is cured properly so that it gives a good mechanical support for the sample in the brass ring. Then the cut disks are grinded from both sides using SiC paper. The rough cutting surfaces from step 5 are then polished away by consecutively using 1200, 2400 and 4000 grit paper on both sides. For the higher grit papers, 2400 and 4000 grit, isopropanol has been used, but other non-reactive liquids could suffice as well. It is tried to remove approximately an equal amount of material from both sides, particularly grinding in the direction of the glue line. Also, if the Si substrate contained cracks which were too severe, another disk is selected.

Step 7 entails dimple grinding of the $t \sim 100$ μm TEM disks. This is done to further remove material from the substrate to speed up the ion-milling process in step 8. Figure 2.13 on the left shows a typical dimple grinder, from the Gatan company, and Figure 2.13 on the right the cross-sectional geometry. For the current specimen preparation recipe the TEM disks are dimpled from both sides to provide a thickness of $\sim$ 20 μm in the center of the disk. In the current geometry, if the thickness $t = 100$ μm, the disk should be dimpled on both sides with a depth $d = 40$ μm. Equation 2.13 gives an expression of the maximum dimple depth when one wants to avoid grinding the brass ring, which could be used in the design. When the dimpling process is finished the specimen should be inspected that it has not detached from the brass support. Also, before proceeding with the ion-milling step, the specimen should be rinsed with acetone and isopropanol.
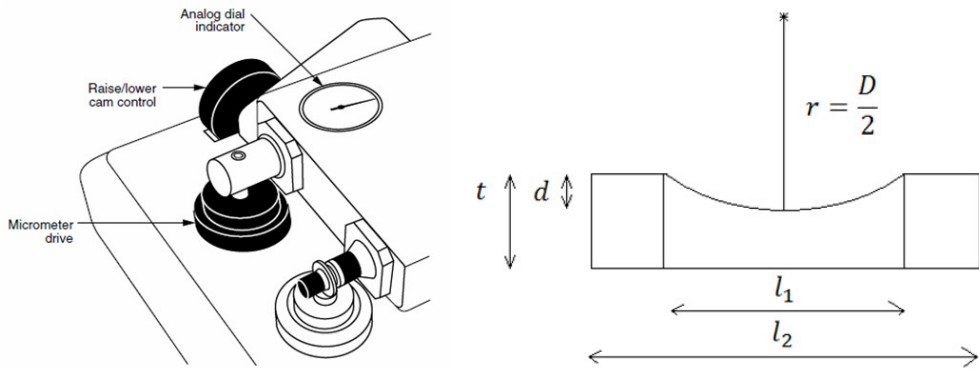
Figure 2.13: *Dimple grinding step. The image on the left shows a typical dimple grinding instrument. The schematic on the right shows the cross-sectional geometry of the TEM disk.*

$$d = \frac{D}{2}(1 - \sin(\cos^{-1}\frac{l_1}{D})) \tag{2.13}$$

The final steps 8 and 9 are Ar ion-milling and ion-polishing of the specimen to obtain a wedge, in which region the specimen is electron transparent. Ion-milling has been performed using a Gatan PIPS II instrument shown in Figure 2.14. Typical milling angles used are in the order of $\theta = 6°$ at an accelerating voltage of $V = 4$ kV till a hole appeared in the specimen. Then fine-polish and remove the residual amorphous damage typical step-like programs were run with smaller voltages of e.g. V = 3 kV, 2 kV, 1 kV, 0.5 kV, 0.2 kV and 0.1 kV using longer polishing times for each consecutive step. The milling and polishing angles should not be too low as to prevent shadowing effects from the brass support. If the total thickness of the TEM disk is $t = 100$ μm, Equation 2.14 indicates that the milling angle should be at least above $\theta = 2.7°$.
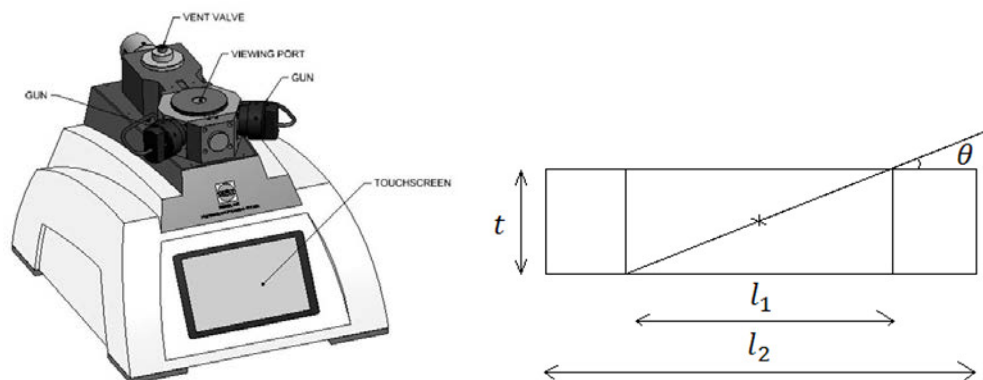
Figure 2.14: *Ion-milling and ion-polishing. The left shows an image of the Gatan PIPS II ion-mill and the right shows a schematic of the cross-sectional TEM disk geometry.*

$$\theta = tan^{-1}\frac{t}{l_1} \qquad\qquad (2.14)$$

An important note to mention about the ion-milling process in step 8 is about single- and double-sector ion-milling modes, of which the schematics are shown in Figure 2.15. This is necessary because the corners of the cross-sectional parts of the specimen tend to be sputtered away more easily, resulting in different shapes of the final wedges.[32] What typically happens for double-sector ion-milling is that the wedge becomes actually blunter than the set angle of $\theta = 6°$ and that therefore a lot of material is redeposited in the region of interest. To prevent this, the procedure by Dieterle et al.[32] is advisable, in which the specimen is milled in single-sector mode thill the milling of the corner is sufficiently progressed and then turned around 180° to continue this step. Figures 2.16 and 2.17 show examples of the initial holes which were obtained with single-sector and double-sector ion-milling as seen in the SEM SE mode, respectively. It can clearly be observed that the holes have different geometries. It can also be deduced that the wedge for the double-sector milled specimen is blunter because the morphology of the region of interest is different from the remainder of the overall sputtered surface. Also, even though the double-sector specimen seems to be more regular, it is much thicker and

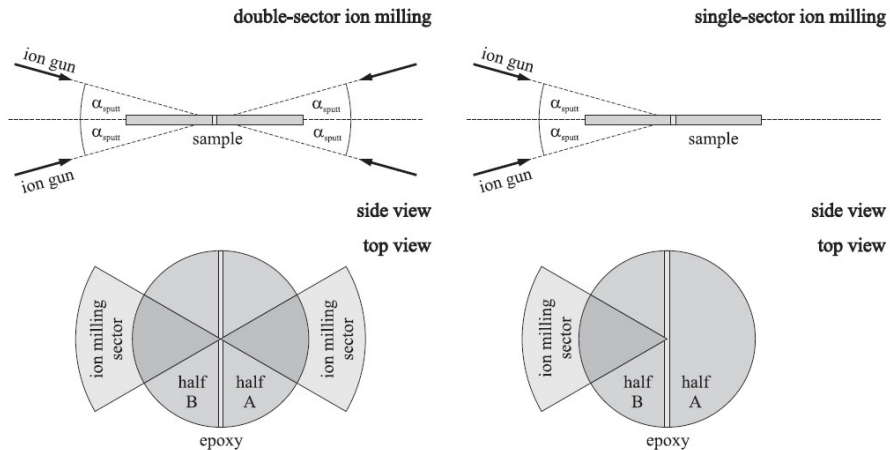typically contains re-deposition of sputtered materials, making it of lesser quality for TEM analysis.

Figure 2.15: *Side-view and top-view of the double- and single-sector ion-milling geometries. Adapted from Dieterle et al.[32]*

Figure 2.18 on the left then shows the final TEM specimen which results from this preparation procedure and on the right a BF TEM overview of the region of interest. The thin film of study is seen by the indicated black line.
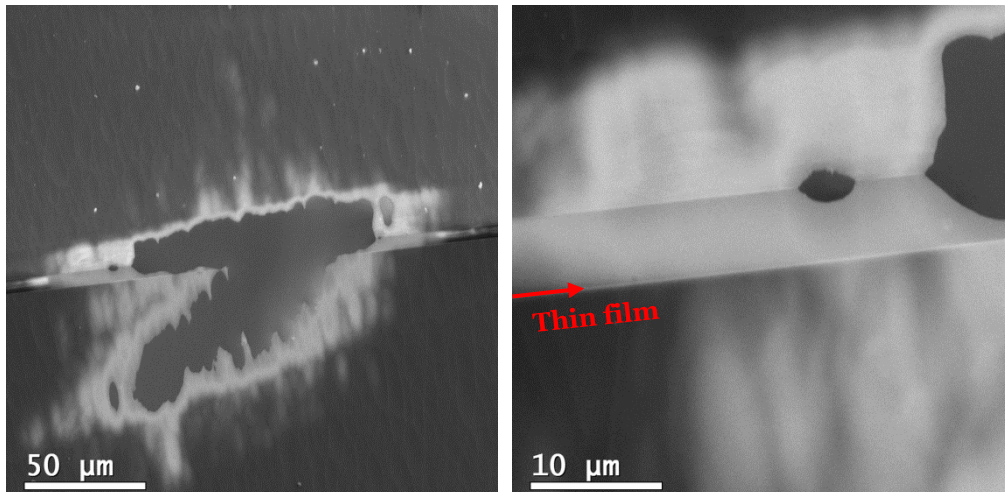

Figure 2.16: *Example of initial hole of a single-sector ion-milled TEM specimen. The left shows an SEM micrograph of the entire hole and the right shows a zoom-in of the part with the region of interest. The thin film is visible as a bright line between the Si substrate and epoxy and is indicated by the red arrow.*
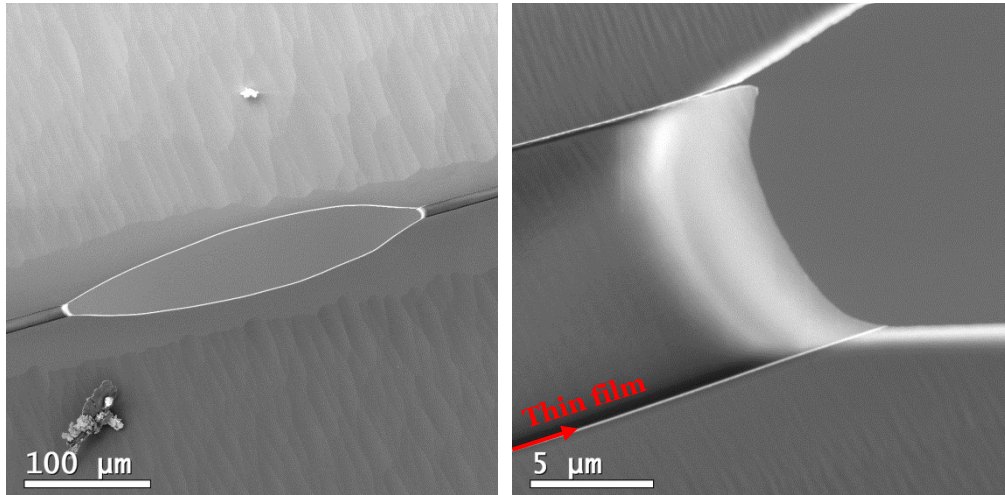
Figure 2.17: *Example of initial hole of a double-sector ion-milled TEM specimen. The left shows an SEM micrograph of the entire hole and the right shows a zoom-in of the part with the region of interest. The thin film is visible as a bright line between the Si substrate and epoxy and is indicated by the red arrow.*
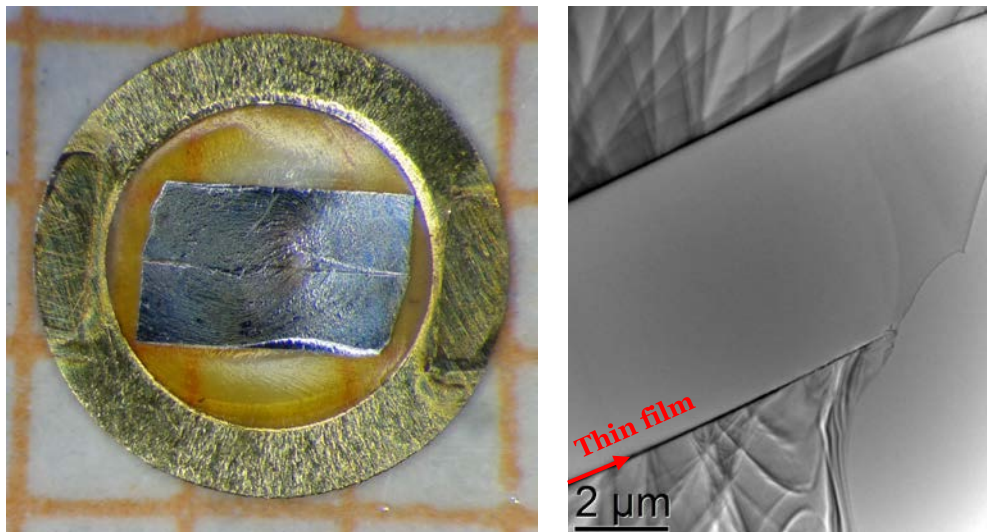

Figure 2.18: *Example of the final TEM cross-sectional specimen in Figure 2.16. The left shows an optical micrograph of a 3 mm disk which is ready for TEM analysis and the right shows a BF TEM overview of the region of interest. The thin film appears as a dark line*

2.2.2 Plan-view method used for this thesis

The plan-view specimen preparation method is a bit simpler and contains fewer steps compared with the cross-sectional method. The consecutive steps for the plan-view method are listed below. A design of the plan-view specimen is shown in Figure 2.19.

1. Measuring and logging the physical dimension of the thin film sample.
2. Cleaving or cutting the sample in ~ 2 mm × 2 mm strips.
3. Gluing the strips to Cu rings with round or oval holes.
4. Mechanical grinding of scaffold till ~100 μm thickness.
5. Dimple grinding of the scaffold on one side.
6. Waxing a thin piece of glass to the scaffold.
7. Ar ion-milling till a hole is visible.
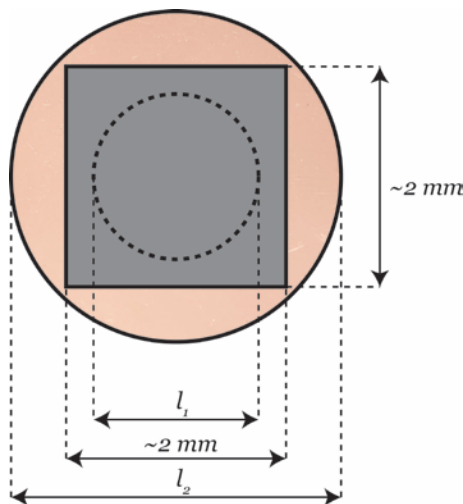8. Lower voltage ion-polishing.

Figure 2.19: Design of plan-view TEM specimen out of thin film samples. The specimen consists of the sample with Si substrate and copper support ring.

Step 1 and step 2 are similar as for the cross-sectional method described in section 2.2.1, only with slightly different dimensions. The specimen is cleaved into ~ 2 mm × 2 mm strips, taking into account the preferential cleaving directions of the Si(111) substrate.[31]

In step 3 a 40 μm thick Cu ring is glued on the film-side of the 2 mm × 2 mm strips with the polished side on the film-side. Here, it is important not to spill epoxy on the center part of the sample, as this will be the region of interest. In case that this is covered with epoxy, it is better to remove it using acetone redo the procedure again. Then the specimen is cured in accordance to the description of the glue producer.

For step 4 the specimen is grinded down to a thickness of ~100 μm thickness. This includes the ~40 μm Cu ring, ~10 μm epoxy and ~50 μm sample using progressively 1200, 2400 and 4000 grit SiC paper. Also here, for the 2400 and 4000 grit paper isopropanol is used for better quality polishing.

In step 5 the specimen is dimpled ~40 μm deep to obtain a thickness of ~10 μm in the center of the dimple. Care should be taken in this step, as the specimen becomes very thin and can easily break.

For steps 6 till 8 it is important to cover the film-side with a glass plate using wax, in order to prevent material redeposition on the sample of interest that would otherwise occur during only top-side milling. Steps 7 and 8 are then quite similar as for the cross-sectional method in section 2.2.1, but using only double-sector ion-milling from the top (the substrate side). The specimen is milled at $\theta = 6°$ at $V = 4$ kV till a hole is visible and polished using step-wise lower voltages and longer milling times. When the specimen is finished, the waxed glass plate is removed carefully on the hot plate and rinsed in acetone and isopropanol. To evaporate all the liquid the specimen in the end is heated at 100 °C for a couple of minutes.

2.3 References

1.   Lane, N. The unseen world: reflections on Leeuwenhoek (1677) 'Concerning little animals'. *Phil Trans R Soc B* **370,** 20140344 (2015).
2.   Williams, D. B. & Carter, C. B. *Transmission Electron Microscopy*. (Springer, 2009).
3.   Ruska, E. The Development of the Electron Microscope and of Electron Microscopy (Nobel Lecture). *Angew. Chem. Int. Ed. Engl.* **26,** 595–605 (1987).
4.   Gass, M. H. *et al.* Free-standing graphene at atomic resolution. *Nat. Nanotechnol.* **3,** 676–681 (2008).
5.   Ishikawa, R. *et al.* Direct imaging of hydrogen-atom columns in a crystal by annular bright-field electron microscopy. *Nat. Mater.* **10,** 278–281 (2011).
6.   Muller, D. A. Practical STEM: More than Z Contrast. (2006).

7. Karpinsky, O. G., Shelimova, L. E., Kretova, M. A. & Fleurial, J.-P. An X-ray study of the mixed-layered compounds of $(GeTe)_n(Sb_2Te_3)_m$ homologous series. *J. Alloys Compd.* **268,** 112–117 (1998).

8. Yamada, N. & Matsunaga, T. Structure of laser-crystallized $Ge_2Sb_{2+x}Te_5$ sputtered thin films for use in optical memory. *J. Appl. Phys.* **88,** 7020–7028 (2000).

9. Matsunaga, T. & Yamada, N. Structural investigation of $GeSb_2Te_4$ A high-speed phase-change material. *Phys. Rev. B* **69,** 104111 (2004).

10. Matsunaga, T., Yamada, N. & Kubota, Y. Structures of stable and metastable $Ge_2Sb_2Te_5$, an intermetallic compound in $GeTe–Sb_2Te_3$ pseudobinary systems. *Acta Crystallogr. B* **60,** 685–691 (2004).

11. Matsunaga, T. *et al.* Structural investigation of $Ge_3Sb_2Te_6$, an intermetallic compound in the $GeTe–Sb_2Te_3$ homologous series. *Appl. Phys. Lett.* **90,** 161919 (2007).

12. Urban, P. *et al.* Temperature dependent resonant X-ray diffraction of single-crystalline $Ge_2Sb_2Te_5$. *CrystEngComm* **15,** 4823–4829 (2013).

13. Kooi, B. J. & Hosson, J. T. M. D. Electron diffraction and high-resolution transmission electron microscopy of the high temperature crystal structures of $Ge_xSb_2Te_{3+x}(x=1,2,3)$ phase change material. *J. Appl. Phys.* **92,** 3584–3590 (2002).

14. Rotunno, E., Lazzarini, L., Longo, M. & Grillo, V. Crystal structure assessment of Ge–Sb–Te phase change nanowires. *Nanoscale* **5,** 1557–1563 (2013).

15. Ross, U., Lotnyk, A., Thelander, E. & Rauschenbach, B. Microstructure evolution in pulsed laser deposited epitaxial Ge-Sb-Te chalcogenide thin films. *J. Alloys Compd.* **676,** 582–590 (2016).

16. Lotnyk, A., Ross, U., Bernütz, S., Thelander, E. & Rauschenbach, B. Local atomic arrangements and lattice distortions in layered Ge-Sb-Te crystal structures. *Sci. Rep.* **6,** 26724 (2016).

17. Mio, A. M. *et al.* Chemical and structural arrangement of the trigonal phase in GeSbTe thin films. *Nanotechnology* **28,** 065706 (2017).

18. Zhang, B. *et al.* Element-resolved atomic structure imaging of rocksalt $Ge_2Sb_2Te_5$ phase-change material. *Appl. Phys. Lett.* **108,** 191902 (2016).

19. McCaffrey, J. P., Phaneuf, M. W. & Madsen, L. D. Surface damage formation during ion-beam thinning of samples for transmission electron microscopy. *Ultramicroscopy* **87,** 97–104 (2001).

20. McCaffrey, J. P. Small-angle cleavage of semiconductors for transmission electron microscopy. *Ultramicroscopy* **38,** 149–157 (1991).

21. McCaffrey, J. P. Improved TEM samples of semiconductors prepared by a small-angle cleavage technique. *Microsc. Res. Tech.* **24,** 180–184 (1993).

22. Walck, S. D. & McCaffrey, J. P. The small angle cleavage technique applied to coatings and thin films. *Thin Solid Films* **308–309,** 399–405 (1997).

23. Mayer, J., Giannuzzi, L. A., Kamino, T. & Michael, J. TEM Sample Preparation and FIB-Induced Damage. *MRS Bull.* **32,** 400–407 (2007).

24. Langford, R. M. & Petford-Long, A. K. Preparation of transmission electron microscopy cross-section specimens using focused ion beam milling. *J. Vac. Sci. Technol. A* **19,** 2186–2193 (2001).

25. Giannuzzi, L. A. & Stevie, F. A. A review of focused ion beam milling techniques for TEM specimen preparation. *Micron* **30,** 197–204 (1999).

26. Rubanov, S. & Munroe, P. R. FIB-induced damage in silicon. *J. Microsc.* **214,** 213–221 (2004).

27. Lotnyk, A. *et al.* Focused high- and low-energy ion milling for TEM specimen preparation. *Microelectron. Reliab.* **55,** 2119–2125 (2015).

28. Kato, N. I. Reducing focused ion beam damage to transmission electron microscopy samples. *J. Electron Microsc. (Tokyo)* **53,** 451–458 (2004).

29. Liu, Y., Wang, R., Guo, X. & Dai, J. A cross-sectional TEM sample preparation method for films deposited on metallic substrates. *Mater. Charact.* **58,** 666–669 (2007).

30. Dürr, A. C., Schreiber, F., Kelsch, M. & Dosch, H. Optimized preparation of cross-sectional TEM specimens of organic thin films. *Ultramicroscopy* **98,** 51–55 (2003).

31. Pérez, R. & Gumbsch, P. Directional Anisotropy in the Cleavage Fracture of Silicon. *Phys. Rev. Lett.* **84,** 5347–5350 (2000).

32. Dieterle, L., Butz, B. & Müller, E. Optimized Ar⁺-ion milling procedure for TEM cross-section sample preparation. *Ultramicroscopy* **111,** 1636–1644 (2011).